nature chemistry

ARTICLES

https://doi.org/10.1038/s41557-021-00787-y

Check for updates

Aqueous interphase formed by CO_2 brings electrolytes back to salt-in-water regime

Jinming Yue[1,2], Jinkai Zhang[3], Yuxin Tong[1,2], Ming Chen[3], Lilu Liu[1], Liwei Jiang[1,2], Tianshi Lv[1,2], Yong-sheng Hu[1], Hong Li[1], Xuejie Huang[1], Lin Gu[1], Guang Feng[3], Kang Xu[4]✉, Liumin Suo[1,2,5]✉ and Liquan Chen[1]

Super-concentrated water-in-salt electrolytes make high-voltage aqueous batteries possible, but at the expense of high cost and several adverse effects, including high viscosity, low conductivity and slow kinetics. Here, we observe a concentration-dependent association between CO_2 and TFSI anions in water that reaches maximum strength at 5 mol kg^{-1} LiTFSI. This TFSI–CO_2 complex and its reduction chemistry allow us to decouple the interphasial responsibility of an aqueous electrolyte from its bulk properties, hence making high-voltage aqueous Li-ion batteries practical in dilute salt-in-water electrolytes. The CO_2/salt-in-water electrolyte not only inherits the wide electrochemical stability window and non-flammability from water-in-salt electrolytes but also successfully circumvents the numerous disadvantages induced by excessive salt. This work represents a deviation from the water-in-salt pathway that not only benefits the development of practical aqueous batteries, but also highlights how the complex interactions between electrolyte components can be used to manipulate interphasial chemistry.

In the era before Li-ion batteries, water was a universal electrolyte solvent in most electrochemical devices, including batteries[1–7], supercapacitors[8,9], CO_2 electrochemical reduction devices[10,11] and electroplating devices[12,13], providing excellent kinetic performances such as fast charging and high rate capability[14,15] as well as low cost. Indeed, all these aqueous devices usually operate at low voltages, confined by the narrow electrochemical stability window of water[16] and serious hydrogen evolution, without the kinetic protection from the solid–electrolyte interphase (SEI) as found in a non-aqueous electrolyte[17–19]. Recently, such confinement by the narrow electrochemical stability window was breached by the breakthrough of a water-in-salt (WIS) electrolyte, which employs super-concentrated lithium salt (21 m lithium bistrifluoromethane sulfonylimide, or LiTFSI) in H_2O and achieved a window of ~3.0 V due to the formation of an interphase in aqueous media[2].

Super-concentrated $LiNO_3$ electrolyte has been used for decades in early attempts at aqueous Li-ion batteries[20], but an interphase was never formed by those electrolytes, to the best of our knowledge. Apparently, the anion chemistry, in addition to its high concentration, is a key factor to induce the formation of an aqueous interphase. Our previous studies have revealed interphasial chemistry formed by WIS electrolyte, such as mixtures of LiF, Li_2O and Li_2CO_3, which should have originated from the reduction of TFSI as well as the dissolved gaseous species (O_2 and CO_2)[21]. While LiF must be contributed by the fluorinated anion, one cannot reasonably explain why the interphase cannot form in other super-concentrated electrolytes based on inorganic anions ($LiNO_3$ and Li_2SO_4), even though both O_2 and CO_2 already exist therein as sources for Li_2O and Li_2CO_3 (refs. [22–24]).

To resolve this paradox, we looked into how the dissolved gases affect the reduction of WIS components (that is, water and TFSI). We discovered that WIS has a very high selective affinity towards CO_2, benefitting from the unique association chemistry between CO_2 and LiTFSI, which routine gas purging is unable to remove. The unusually high solubility of CO_2 in WIS seemed to be directly responsible for the Li_2CO_3-containing interphase. Leveraging this discovery, we introduced CO_2 as an interphase-forming additive for aqueous electrolytes so that the interphase responsibility is decoupled from the main mission of the bulk electrolyte; that is, fast ion transport and super-high concentration is no longer necessary. The CO_2-induced interphase provides a wide electrochemical window comparable to that of WIS electrolyte at only 5 m LiTFSI (m, moles per kilogram), thus relieving the high cost incurred by excessive usage of LiTFSI. Besides this advantage, the much-diluted electrolyte also offers additional benefits that WIS electrolyte does not possess, such as excellent ion conductivity, low viscosity and a wide service temperature range. The aqueous Li-ion cells based on this electrolyte exhibit excellent performances that are dictated by kinetics, including the rate performance and tolerance against low temperature (−40 °C), as well as a high mass-loading thick electrode. The revealed TFSI–CO_2 interaction allows the important correction to the super-high-concentration approach to high-voltage aqueous electrolytes with these direct benefits on a practical aqueous Li-ion battery. In addition, on a fundamental level, understanding the interactions between important gaseous species and aqueous electrolytes, as well as the reduction chemistry of these gaseous species in the battery environment, might offer new opportunities beyond just battery materials and chemistries.

[1]Beijing Advanced Innovation Center for Materials Genome Engineering, Key Laboratory for Renewable Energy, Beijing Key Laboratory for New Energy Materials and Devices, Beijing National Laboratory for Condensed Matter Physics, Institute of Physics, Chinese Academy of Sciences, Beijing, China. [2]Center of Materials Science and Optoelectronics Engineering, University of Chinese Academy of Sciences, Beijing, China. [3]State Key Laboratory of Coal Combustion, School of Energy and Power Engineering, Huazhong University of Science and Technology, Wuhan, China. [4]Battery Science Branch, Sensor and Electron Devices Directorate, US Army Research Laboratory, Adelphi, MD, USA. [5]Yangtze River Delta Physics Research Center Co. Ltd, Liyang, China. ✉e-mail: conrad.k.xu.civ@mail.mil; suoliumin@iphy.ac.cn

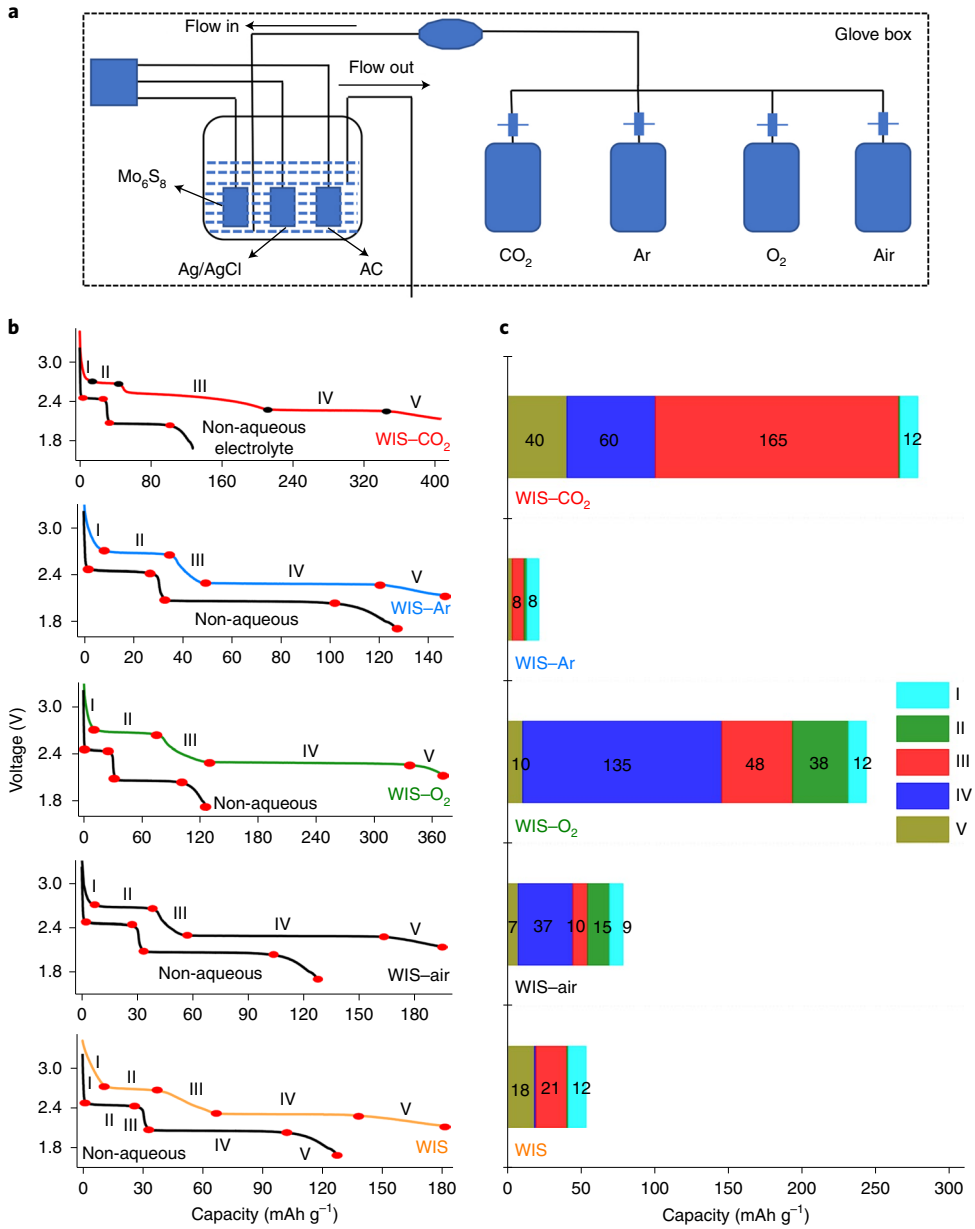

Fig. 1 | Quantitative analysis of the contribution to the initial discharge capacity in various WIS electrolytes. a, Schematic diagram of the operating environment of the three-electrode device. AC, active carbon. **b**, The voltage profiles of Mo_6S_8 electrodes during the initial discharge in three-electrode devices supported by WIS (21 m LiTFSI) that has been saturated by various gases (CO_2, Ar, O_2 or air). Non-aqueous electrolyte assembled in a coin cell was used as a reference. **c**, The corresponding incremental capacities at different discharge stages (I–V) as referenced to the non-aqueous coin cell, that is, contributed by the reduction of the different gases.

Results and discussion

Identifying the influence of dissolved CO_2 on the interphasial chemistry. Interphase formation in WIS electrolyte originates from the simultaneous reductions of the TFSI anion and dissolved gases[21]. In the battery environment, however, the characteristic reduction potentials for the anion and dissolved gases cannot be precisely differentiated and quantified due to the relatively insignificant mass corresponding to interphase formation when compared with the overall Faradaic process. To resolve this challenge, we designed a three-electrode device supplied with a continuous gas flow so that the effect of these gases can be magnified. All experiments were carried out in an Ar-filled glove box, and the cells were prepurged with the objective gas to eliminate the other residual gases in the electrolyte. Moreover, the three-electrode device with Mo_6S_8 as the working electrode and Ag/AgCl as the reference electrode can monitor the precise potential of all electrochemical reactions corresponding to the redox potentials of active electrode materials, gas reduction and decomposition of electrolyte components (Fig. 1a; detailed descriptions in the Methods). The irreversible Faradaic reactions, including interphase formation and electrolyte decomposition, can be identified by the potential–capacity relationship from the charge–discharge curve (Fig. 1b). The contributions from these processes to capacity during the initial discharge were quantitatively analysed in various WIS electrolytes (Fig. 1c). The capacity achieved by WIS in the three-electrode cell (180 mAh g^{-1}) is higher not only than the non-aqueous electrolyte but also than itself when placed in coin cells (103 mAh g^{-1}, against the theoretical capacity of Mo_6S_8, 128 mAh g^{-1} (ref. [2]); Supplementary Figs. 1–5). Hence the gas

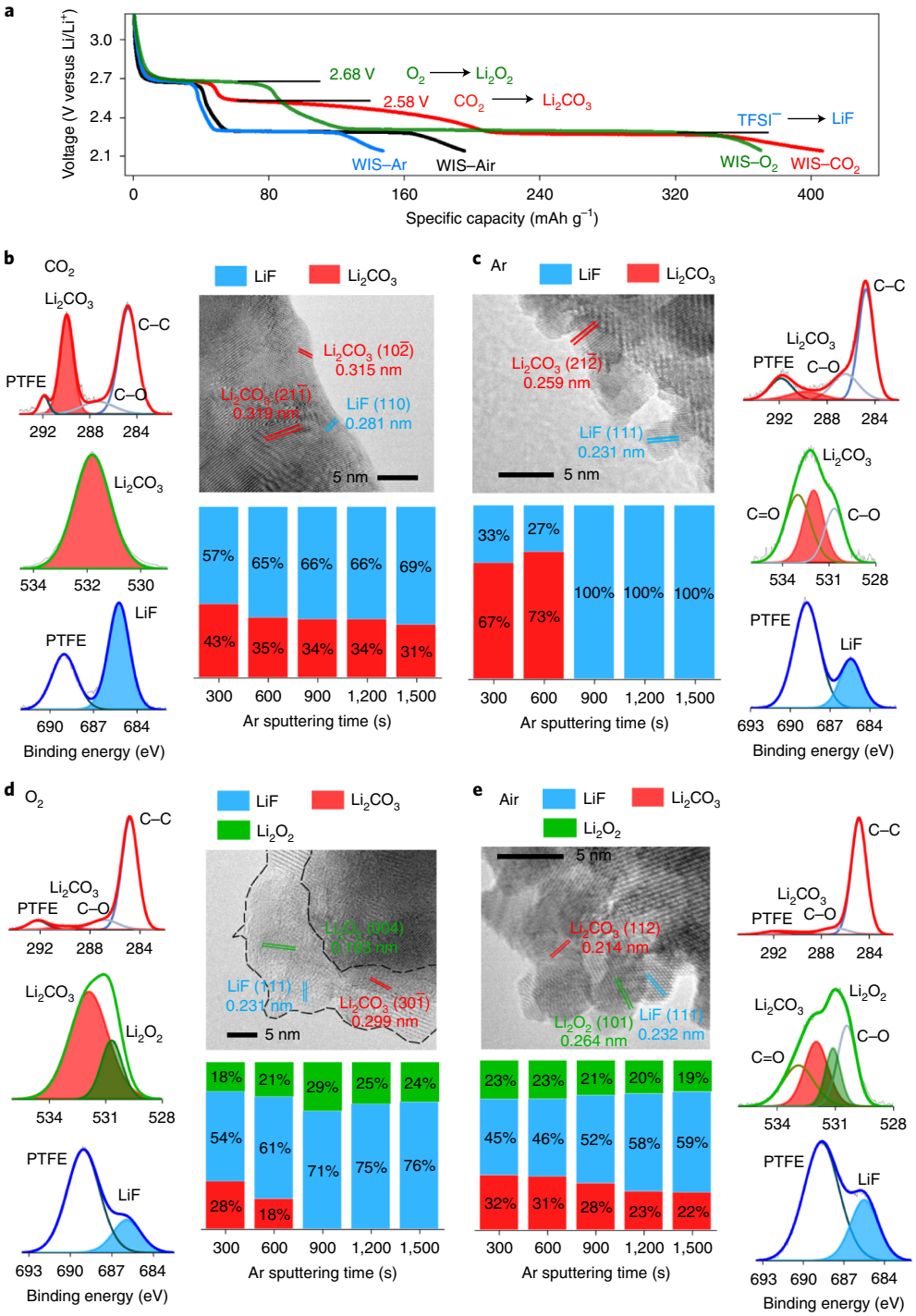

Fig. 2 | The evaluation of the SEI on the Mo_6S_8 electrode in WIS electrolyte (21 m LiTFSI) saturated with various gases in the three-electrode device. **a**, The first charge–discharge profiles of Mo_6S_8 electrodes with WIS are saturated by the different gas flows. **b**–**e**, The XPS spectra characterize the interphasial chemistry and structure of the cycled Mo_6S_8 electrodes in those electrolytes with the Ar ion sputtering and TEM images (CO_2 (**b**), Ar (**c**), O_2 (**d**) and air (**e**)). PTFE, polytetrafluoroethylene.

reduction as the parasitic reaction depends on the absolute amount of dissolved gas in WIS or indirectly on the amount of electrolyte used, because the amount of electrolyte in the three-electrode device (6,500 µl) is about 80 times as high as in the coin cell (80 µl).

This argument was further confirmed because the capacity further increases to 195.4 mAh g^{-1} when WIS electrolyte was saturated with air, while the capacity decreased to 147 mAh g^{-1} when WIS electrolyte was saturated with Ar. In particular, WIS electrolyte saturated with both CO_2 and O_2 achieved capacities of 406.7 mAh g^{-1} and 370.8 mAh g^{-1}, respectively. In other words, both CO_2 and O_2 make leading contributions to the irreversible capacities during the initial lithiation process of the anode material[21]. The most significant increase in capacity occurs in stage III (Fig. 1b) for WIS electrolyte saturated with CO_2 (165 mAh g^{-1}) and stage IV (Fig. 1b) for WIS electrolyte saturated with air and O_2. Therefore, CO_2 is the most electrochemically sensitive gas against the reduction, with a

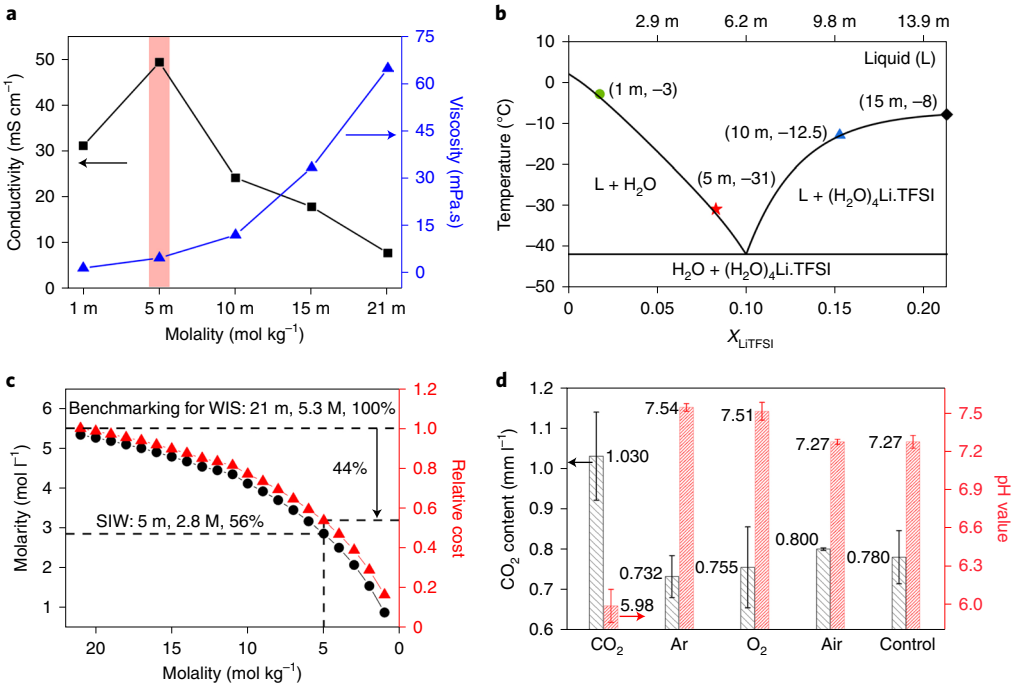

Fig. 3 | The physicochemical properties of 5 m LiTFSI solution. a, The comparison of viscosity and conductivity varies with concentration; 5 m shows a high conductivity and lower viscosity, as indicated by the pink vertical line. **b**, Binary phase diagram of LiTFSI–H_2O according to the differential scanning calorimetry of 1 m, 5 m, 10 m and 15 m electrolyte; and the value of 1 m originated from our previous work[39] (where m is molality, in moles per kilogram, and X_{LiTFSI} is the LiTFSI molar fraction in the LiTFSI-H_2O solution). The 5 m shows a lower liquid temperature of −31 °C. **c**, The price trends and a correspondence relationship between molality (m, moles per kilogram) and molarity (M, moles per litre) from 21 m to 1 m. **d**, The comparison of CO_2 content and pH value of 5 m LiTFSI solution after the different gas flows (CO_2, Ar, O_2 or air); the control indicates no treatment. All the samples were measured three times ($n = 3$) to get the mean value, and the standard deviation error bar is marked.

reducing potential in the range of ~2.6–2.2 V versus Li/Li$^+$. O_2 also has a strong tendency to reduce in the range of ~2.7–2.3 V versus Li/Li$^+$ (Fig. 2a). Those electrochemical processes ($CO_2 \rightarrow Li_2CO_3$, 2.58 V versus Li/Li$^+$; $O_2 \rightarrow Li_2O_2$, 2.68 V versus Li/Li$^+$; Fig. 2a) are basically consistent with the respective thermodynamic potentials[25,26]. Similarly, the second plateau of Mo_6S_8 extends obviously in WIS electrolytes saturated with CO_2, air and O_2, all of which contribute to the TFSI anion reduction.

Figure 2a compares the four discharge curves of the Mo_6S_8 half-cell in the presence of various gases (CO_2, Ar, O_2 and air). The discharge profile of the WIS–CO_2 electrolyte demonstrates a noticeable slope of CO_2 reduction below 2.58 V versus Li/Li$^+$. In WIS–O_2 electrolyte, a similar reduction is also observed but at a slightly higher potential of 2.68 V versus Li/Li$^+$. Meanwhile, since the TFSI anion reduction starts at a potential lower than 2.9 V versus Li/Li$^+$ (ref. [21]), it precedes both the CO_2 and O_2 processes. The simultaneous reduction of all these species, dissolved gases (CO_2 or O_2) and TFSI anion, contribute to interphasial chemistries, while the WIS–CO_2 system with its highest capacity of 406.7 mAh g^{-1} should dominate this contribution, as subsequently confirmed by scanning electron microscopy (SEM) (Supplementary Fig. 6). X-ray photoelectron spectroscopy (XPS) results revealed the main chemical components on the electrode surface to be Li_2CO_3 and LiF, whose corresponding lattice distances are marked by red and blue, respectively, in high-resolution transmission electron microscopy (TEM) images (Fig. 2b). With stepwise Ar$^+$ sputtering, the depth profile established that LiF and Li_2CO_3 always coexist during the etching.

In the WIS–O_2 system, in addition to LiF, Li_2O_2 was also detected by XPS spectra (Fig. 2d)[27]. Li_2O_2 can exist stably in WIS electrolytes without reacting with either solvent (water), salt (TFSI) or other components that result from their reduction[28]. More evidence for Li_2O_2 and LiF come from TEM (Fig. 2d). Therefore, we can conclude with confidence that the reduction product of dissolved O_2 is Li_2O_2 instead of the more reduced form Li_2O. This transition from oxides to peroxides in the oxygen reduction chemistry occurring in TFSI$^-$ or triflate-based aqueous electrolytes has been recently attributed to the hydrophobicity introduced by these fluorinated anions[6].

In the WIS–air system, O_2 and CO_2 coexist, so all the products mentioned above were detected in XPS, listed in the order of abundance, they are LiF, Li_2O_2 and Li_2CO_3, whose lattice distances were also identified in TEM. Both Li_2O_2 and Li_2CO_3 show a decreasing trend with the etching time, while LiF shows a reversed trend (Fig. 2e). This should reflect a layered structure of the interphase.

Most impressive is the WIS–Ar system, which, after prolonged Ar prepurging as well as continuous Ar flow during the test, showed Li_2CO_3 still present in XPS (Fig. 2c); the same phenomenon was also discovered in the WIS–CO_2 system. This result strongly implies that simple gas purging can eliminate the dissolved O_2 but not CO_2 from WIS electrolyte. Thus, we suspect that an unknown unique interaction might exist between CO_2 and TFSI that is responsible for the interphase rich in Li_2CO_3 under all circumstances.

The physicochemical properties of CO_2/salt-in-water (SIW) electrolyte. Inspired by this thought, we conceived the idea of using CO_2 as an additive so that we do not have to rely on an extremely high salt concentration for interphase formation. The benefit of avoiding super-high concentration is evident from the 5 m LiTFSI SIW electrolyte, whose high maximum conductivity (49.46 mS cm^{-1}), very low viscosity (4.84 mPa.s; Fig. 3a) and very low liquidus temperature (T_l, −31 °C) that approaches the eutectic point of the system (Supplementary Figs. 7–10 and Fig. 3b)[29]

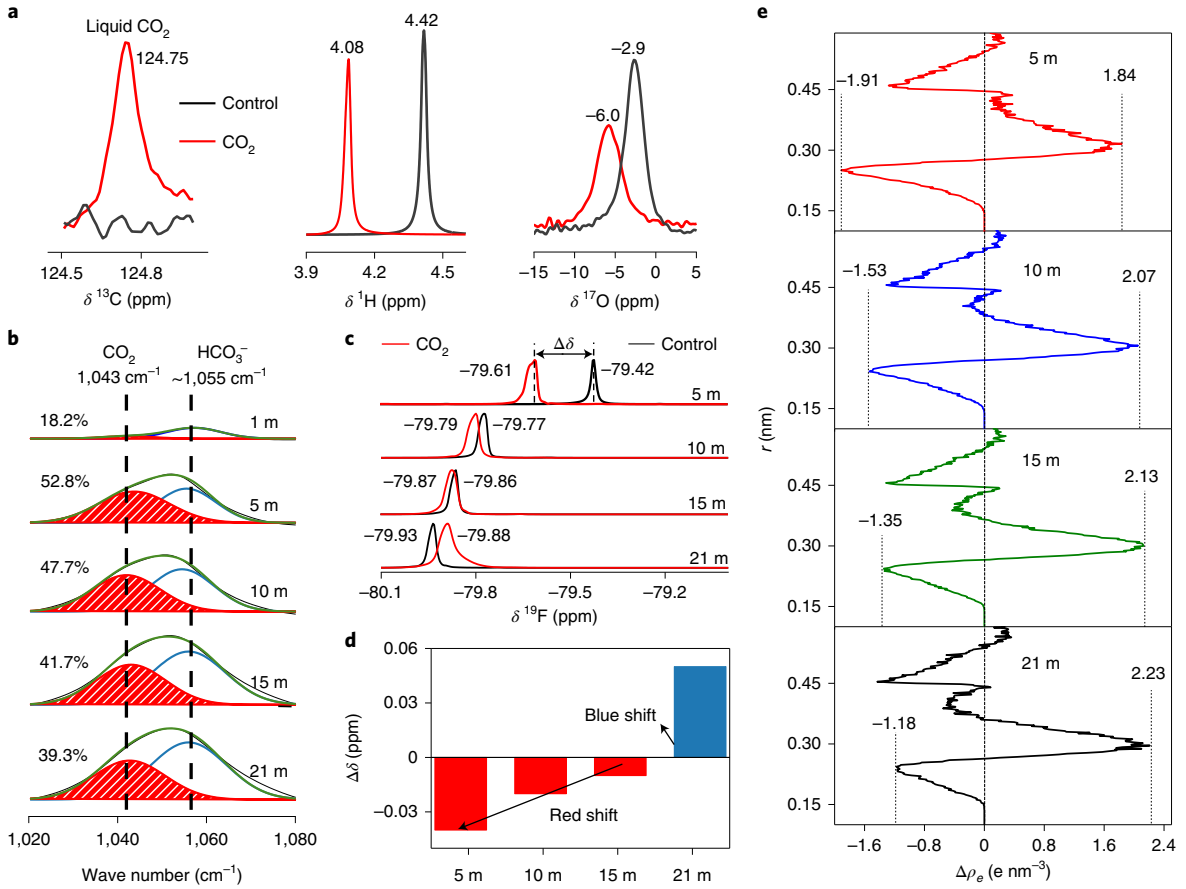

Fig. 4 | The interaction between CO_2 and the TFSI anion before and after treatment with CO_2. **a**, The ^{13}C, ^{1}H and ^{17}O spectra of 5 m SIW electrolyte. **b**, FTIR spectra of different concentrations of electrolyte (1 m, 5 m, 10 m, 15 m and 21 m). **c**,**d**, The ^{19}F NMR spectra and their corresponding chemical shifts. **e**, The molecular dynamics simulation of charge changes around F of the TFSI anion ($\Delta\rho_e = \rho_{e,CO_2-dealt} - \rho_{e,control}$) (where r is the distance from atom F of TFSI anion). In **c**–**e**, one can identify the stronger interaction between CO_2 and the TFSI anion.

promise far superior performances otherwise unavailable from WIS electrolyte. Despite these advantages, our previous works showed that 5 m SIW does not support the electrochemistry of a Mo_6S_8 anode when used alone[21] due to the severe electrolyte decomposition preceding the lithiation of Mo_6S_8. In other words, an interphase failed to form when there were not enough anions in the bulk electrolyte, and ongoing hydrogen evolution prevailed. If the dissolved CO_2 could suppress the hydrogen evolution reaction, then interphasial chemistry could be at least partially decoupled from the salt concentration because an interphase based on the reductions of CO_2 and TFSI could occur at a relatively low salt concentration. Such an aqueous electrolyte would inherit the intrinsic safety from WIS electrolyte while offering far superior kinetics-related performances typical of diluted electrolytes along with significant cost reduction to ~56% (Fig. 3c). Figure 3d shows the pH value and the CO_2 content in 5 m SIW electrolytes after different gas treatments. Upon saturation with CO_2 at 1.03 mm l^{-1} (Supplementary Table 1), the lowest pH value is 5.98, which significantly differs from that of other systems with various gases (Supplementary Table 2), implying that more CO_2 can be dissolved in the electrolyte, whose final hydrogen evolution reaction potential is a slight 0.03 V higher than that in the 5 m SIW electrolyte ((1.67 V versus Li/Li^+) versus (1.64 V versus Li/Li^+); Supplementary Fig. 11); meanwhile, the key properties (ion conductivity and viscosity) are not affected by the dissolution of CO_2, as shown in Supplementary Figs. 12 and 13.

Discovering the interaction between CO_2 and the TFSI anion. We applied nuclear magnetic resonance (NMR) and Fourier transform infrared spectroscopy (FTIR) to probe the interactions of CO_2–water and CO_2–TFSI anion in 5 m SIW electrolyte. The equilibrium of CO_2 dissolution in water is described as $CO_2 + H_2O = H_2CO_3 = H^+ + HCO_3^-$. The HCO_3^- existence is verified by the increased peak intensity of the FTIR peak at around 1,055 cm^{-1} (ref. [30]; Supplementary Fig. 14) and the evident chemical shift of the ^{1}H NMR spectrum[31] (Supplementary Fig. 15). Meanwhile, a new peak appearing at 124.75 ppm (refs. [32,33]) in the ^{13}C NMR spectrum that does not belong to the carbon nuclei in TFSI (~120 ppm)[34] confirms the existence of CO_2 (Fig. 4a). Both ^{1}H and ^{17}O NMR spectra in water have a slight red shift in the presence of CO_2 (Fig. 4a), suggesting a reduced shielding[35] due to an increase of electron density in their surroundings resulting from the interaction of CO_2. Moreover, the FTIR spectra of the LiTFSI solution show an obvious distortion after treatment with CO_2, which can be fitted with two peaks, corresponding to HCO_3^- (~1,055 cm^{-1}) and CO_2 (1,043 cm^{-1}; Fig. 4b). As the fitting results show, the peak area ratio of CO_2 to HCO_3^- with increasing concentration tends to increase first and then decrease, producing a maximum ratio at 5 m (52.8%). Furthermore, the asymmetrical peak of the ^{19}F NMR spectra with the obvious chemical shift shows that the CO_2 strongly affects the charge density around F (Fig. 4c)[36], since electronic density on the TFSI anion favours the association with an electrophilic CO_2 (refs. [37,38]).

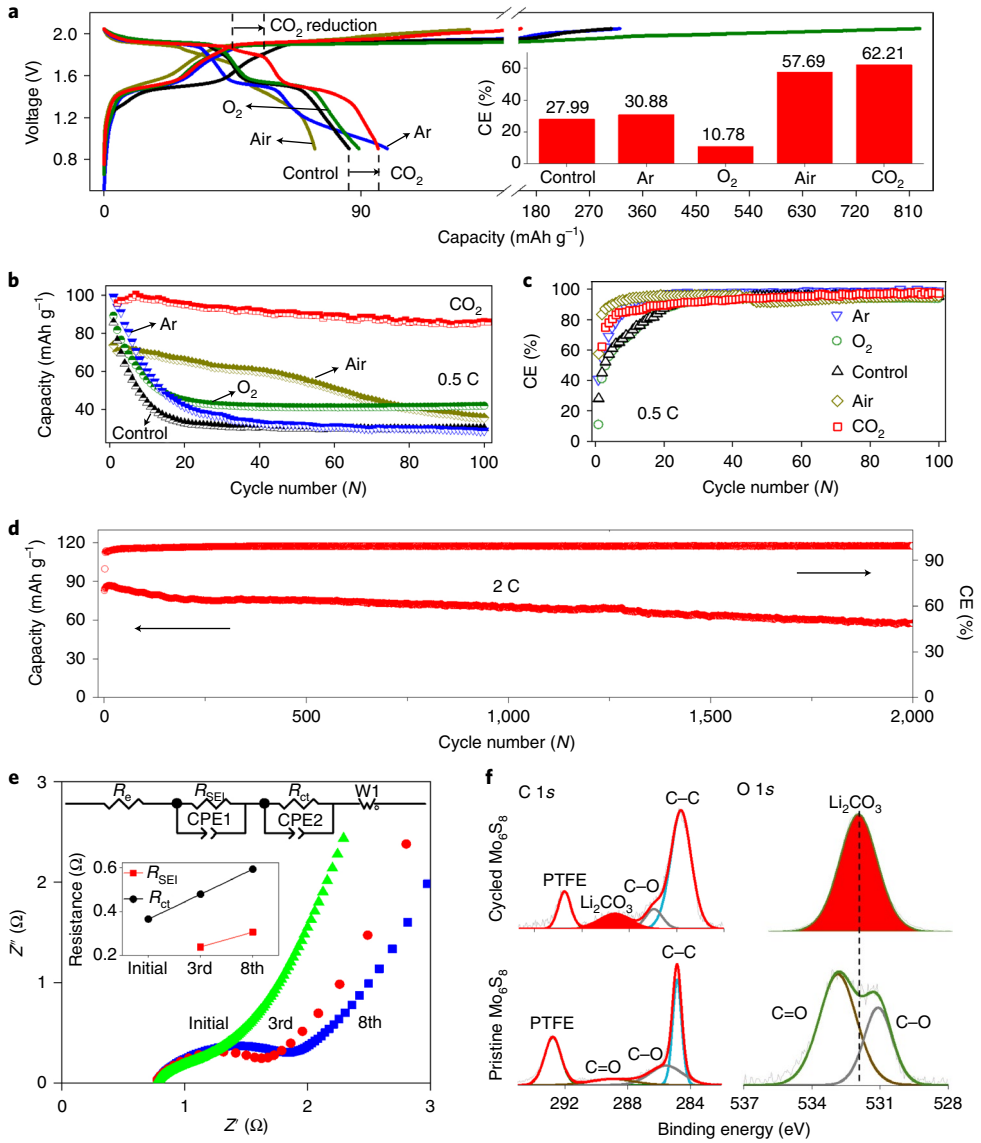

Fig. 5 | The electrochemical performance of an aqueous full-cell ($LiMn_2O_4$/CO_2–SIW/Mo_6S_8). The mass ratio of $LiMn_2O_4$ to Mo_6S_8 is 2:1, and the specific capacity was calculated based on the Mo_6S_8 anode. **a**, The first charge–discharge profiles of CO_2–SIW and other control electrolytes with the 1st CE values in the inset. **b**,**c**, The cycle life at 0.5 C (**b**) with the corresponding CE (**c**). **d**, The cycle life at 2 C. **e**, The Nyquist plots of the full-cell in CO_2–SIW electrolyte with corresponding fitting results of the electrochemical impedance spectra (where Z' is the real part of the impedance, Z'' is the imaginary part of the impedance, R_e is the electrolyte resistance, R_{SEI} is the SEI formation resistance, R_{ct} is the charge transfer resistance, CPE is the constant phase angle element, and W1 is the infinite diffusion impedance. **f**, The XPS spectra (C 1s and O 1s) of Mo_6S_8 electrodes before and after cycling.

More interestingly, 5 m SIW electrolyte presents the biggest red shift ($\Delta\delta = -0.15$ ppm) compared with others (10 m, $\Delta\delta = -0.02$ ppm; 15 m, $\Delta\delta = -0.01$ ppm; Fig. 4d), indicating that the association between CO_2 and TFSI reaches its maximum at 5 m (ref. [36]). To further confirm this argument, a molecular dynamics simulation (details in the Methods) was performed to compare the change of charge density around F before and after treatment with CO_2 (Supplementary Figs. 16 and 17). The charge density differences between the control sample and CO_2-treatment sample ($\Delta\rho_e = \rho_{e,CO_2-dealt} - \rho_{e,control}$) are shown in Fig. 4e. The most noticeable changes were marked: as the concentration decreases from 21 m to 5 m, the negative charge density difference decreases from −1.18 to −1.91, and the positive charge density difference decreases from 2.23 to 1.84 accordingly, revealing the strongest electronic density change around F after treatment with CO_2 at 5 m, which is consistent with our NMR results (Fig. 4c,d). Specifically, those changes of negative charge density difference derive from the water molecule (Supplementary Figs. 18–21), and the decrease of the positive charge density change originates from the TFSI anion (Supplementary Figs. 22–25). The above results show that the introduced CO_2 is involved in interactions with both water and the TFSI anion, whose content and existence are highly dependent on the ratio of salt to water and who would cause electronic density changes around F. Interestingly, CO_2 in 5 m SIW exhibits the strongest interaction with the TFSI anion, resulting in a stable and rich state of CO_2 therein that cannot be easily purged away. It is expected that the rich CO_2–SIW electrolyte would be favourable to form the SEI, and that the superior physical–chemical properties in relatively low concentrations (5 m) would be beneficial to enhance the kinetics of batteries.

Evaluating the electrochemical performance of CO_2–SIW electrolyte. The electrochemical performances of 5 m aqueous electrolyte saturated with CO_2 were evaluated in a full-cell constructed

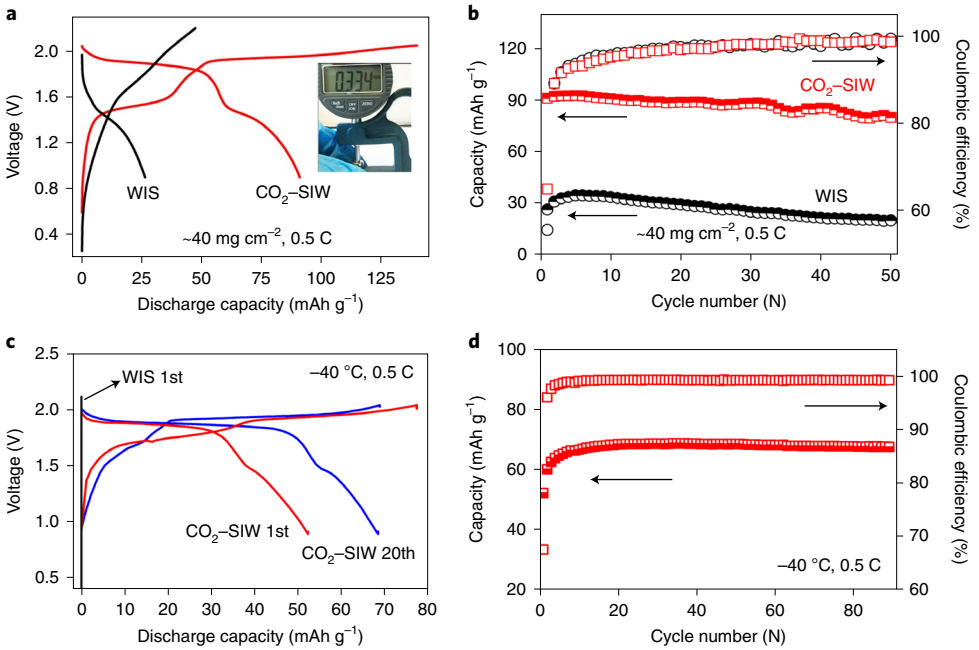

Fig. 6 | The kinetics-determining electrochemical performances of the $LiMn_2O_4$/Mo_6S_8 aqueous full-cell in CO_2–SIW and WIS electrolytes. The mass ratio of $LiMn_2O_4$ to Mo_6S_8 is 2:1, and the specific capacities were calculated based on the Mo_6S_8 anode. **a**,**b**, The first charge–discharge profiles (**a**) and cycling performance (**b**) under a thick electrode (40 mg cm^{-2}, 334 μm) at 0.5 C. **c**,**d**, The first charge–discharge profiles (**c**) and cycling performance (**d**) under low temperature (−40 °C) at 0.5 C.

with $LiMn_2O_4$ as the cathode and Mo_6S_8 as the anode, whose typical charge–discharge profiles were collected by three-electrode cells (Supplementary Figs. 26 and 27). Compared with WIS (Supplementary Fig. 28) and CO_2–WIS, the lower concentrated CO_2–SIW electrolyte (Supplementary Fig. 11) shows higher hydrogen and lower oxygen evolution in an inert Al electrode by linear sweep voltammetry; however, the CO_2–SIW electrolyte is good enough to support the full-cell, benefiting from the formation of the SEI during the charge–discharge process. As shown below, the CO_2–SIW electrolyte has an initial Coulombic efficiency (CE) of 62.21%, and its charge–discharge profile displays an evident CO_2 reduction at around 1.86 V (marked in Fig. 5a). By sharp contrast, the pristine SIW and those saturated with other gases have visible electrolyte decomposition in the irreversible charging process, resulting in lower CE values of 27.99% (SIW), 30.88% (Ar–SIW), 10.78% (O_2–SIW) and 57.69% (air–SIW). Figure 5b,c shows the cycling performances of all SIW electrolytes at 0.5 C, which verifies that the CO_2–SIW electrolyte maintains excellent cycling stability with 90% capacity retention after 100 cycles (initial capacity, 95.94 mAh g^{-1}; 100 cycles, 86.12 mAh g^{-1}), pronouncedly different from pristine SIW or SIW saturated with other gases, none of which survives more than 20 cycles except for the air-containing SIW, which may be due to the CO_2 from the air. In addition, the CO_2–SIW electrolyte achieves a long-term cycle life of up to 2,000 cycles at a higher rate (2 C) with retention of almost 70% (Fig. 5d), indicating that both cathode and anode have excellent chemical and electrochemical stability in CO_2–SIW electrolyte. The cycled $LiMn_2O_4$ cathode after 15 cycles in the three-electrode device (Supplementary Fig. 29) presents very low Mn dissolution (as shown by inductively coupled plasma mass spectrometry, 18.4 μg ml^{-1}), good crystal structure stability (as shown by X-ray diffraction, Supplementary Fig. 30) and unchanged electrode morphologies (as shown by SEM, Supplementary Fig. 31) without any interphasial formation in the cathode side (as shown by XPS, Supplementary Fig. 32, and TEM, Supplementary Fig. 33). They are marking a dilute aqueous electrolyte that delivers competitive electrochemical performance against the super-concentrated WIS. Furthermore, the CE of CO_2–SIW electrolyte gradually increases to >97% in the following cycles, which is implied by the increasing interfacial resistances after eight cycles in the electrochemical impedance spectroscopy (Fig. 5e). The direct proof for the existence of the SEI was finally provided by XPS. As shown in Fig. 5f, after ten cycles, there were evident peaks of Li_2CO_3 based on both C 1*s* and O 1*s* spectra when compared with the initial electrode, while LiF can also be detected after a 200 s Ar^+ sputtering (Supplementary Fig. 34). This is consistent with our previous knowledge that Li_2CO_3 resides outside while LiF is on the inside of the SEI, an order determined by their respective reduction potentials (TFSI, <2.9 V versus Li/Li$^+$; CO_2, 2.58 V versus Li/Li$^+$). As a reference, 5 m $LiNO_3$ electrolyte saturated with CO_2 was also tested, which induces severe over-charge issues, showing that CO_2 fails to form any interphase (Supplementary Fig. 35). Hence, the unique interaction between CO_2 and SIW might serve as the key to forming interphases.

More impressively, the batteries built with CO_2–SIW offer much better kinetics than those with WIS due to the higher ionic conductivity, lower viscosity and low-temperature tolerance of the former, as evidenced by its resistance, 50% lower than that of WIS (Supplementary Fig. 36). In comparison with WIS, the CO_2–SIW not only shows a better rate capability with a higher retention capacity of 70% at 15 C (Supplementary Fig. 37) but also can access the total capacity from a very thick Mo_6S_8 electrode of >300 μm with the superior, high loading mass of 40 mg cm^{-2} (Fig. 6a), which is nearly twice as much as that of the electrodes used in commercial Li-ion batteries (~100–200 μm). Being capable of using thick electrodes is the key factor that indicates a high energy density can be achieved at the cell level, but in real life, this capability is often limited by the kinetics imposed by electrolytes and interphases. However, in this work, with the benefit of a dilute aqueous electrolyte, batteries built with such a thick electrode exhibit superior cycling stability, delivering an initial

capacity of 90 mAh g^{-1} as well as a retention of 88% after 50 cycles, while a low capacity of 25 mAh g^{-1} was realized in the WIS electrolyte (Fig. 6b). Also, CO_2–SIW could maintain good fluidity at an extreme low temperature of −40 °C (Supplementary Fig. 38), which cannot be achieved in the WIS electrolyte (Fig. 6c); the batteries built with the CO_2–SIW electrolyte exhibit outstanding low-temperature tolerance, with a capacity that stays above 70 mAh g^{-1} at 0.5 C under a temperature of −40 °C (Fig. 6d).

Finally, we attempt to establish a comprehensive electrochemical reduction mechanism of the CO_2–SIW electrolyte as follows: (1) SIW electrolyte has a strong affinity towards CO_2, which links with both water and the TFSI anion, and hence is enriched therein. (2) Such a preferred dissolution of CO_2 tends to reduce into Li_2CO_3 on the anode surface during the discharge process. When compared with the electrochemistry of a Li–CO_2 battery, the reduction potential of CO_2 (2.58 V versus Li/Li^+) is a little lower than the ~2.8 V versus Li/Li^+ as observed in the latter[26], possibly due to the association with the CO_2–TFSI anion interaction, which needs extra energy to break. Because the Li_2CO_3 suppresses the hydrogen evolution reaction on the anode effectively, it also assists in the reduction of the TFSI anion simultaneously. The combination of the CO_2 and TFSI anion reductions enables robust and energetic interphase formation even at low salt concentrations.

Conclusions

In this work, the reduction mechanism of various gases dissolved in WIS electrolyte is investigated using a tailor-made three-electrode device equipped with a continuous gas-flow supply. Combining comprehensive interfacial characterizations, we found a unique interaction between CO_2 and TFSI, which subsequently impacts the electrochemical behaviour and leads to an interphase rich in Li_2CO_3. Leveraging this discovery, we designed a CO_2–SIW electrolyte (CO_2 in 5 m LiTFSI–H_2O), in which CO_2 acts as the interphase formation additive. Such a dilute aqueous electrolyte inherits the wide electrochemical stability window and safety from the WIS electrolyte while successfully circumventing its disadvantages such as slow kinetics, high liquidus temperature and high cost. An aqueous Li-ion cell built with such an electrolyte not only displays a similar voltage tolerance as that of WIS electrolyte but also delivers an excellent rate performance, a superior low-temperature performance (−40 °C) and the capability of accessing high capacity based on a high mass-loading thickness electrode. Besides these benefits in battery performance, the lower concentration also reduces the cost by half. We believe that the discovery of this CO_2–TFSI interaction not only benefits the practical aqueous Li-ion battery by correcting the unsustainable super-high concentration approach but, in a broader context, leads us to understand the once overlooked complex interactions among the electrolyte components and to harness them for interphasial chemistry manipulation.

Online content

Any methods, additional references, Nature Research reporting summaries, source data, extended data, supplementary information, acknowledgements, peer review information; details of author contributions and competing interests; and statements of data and code availability are available at https://doi.org/10.1038/s41557-021-00787-y.

Received: 8 February 2021; Accepted: 13 August 2021;
Published online: 11 October 2021

References

1. Li, W., Dahn, J. R. & Wainwright, D. S. Rechargeable lithium batteries with aqueous electrolytes. *Science* **264**, 1115–1118 (1994).
2. Suo, L. et al. "Water-in-salt" electrolyte enables high-voltage aqueous lithium-ion chemistries. *Science* **350**, 938–943 (2015).
3. Luo, J.-Y., Cui, W.-J., He, P. & Xia, Y.-Y. Raising the cycling stability of aqueous lithium-ion batteries by eliminating oxygen in the electrolyte. *Nat. Chem.* **2**, 760–765 (2010).
4. Yamada, Y. et al. Hydrate-melt electrolytes for high-energy-density aqueous batteries. *Nat. Energy* **1**, 16129 (2016).
5. Yang, C. et al. Aqueous Li-ion battery enabled by halogen conversion–intercalation chemistry in graphite. *Nature* **569**, 245–250 (2019).
6. Sun, W. et al. A rechargeable zinc-air battery based on zinc peroxide chemistry. *Science* **371**, 46–51 (2021).
7. Wu, X. et al. Reverse dual-ion battery via a $ZnCl_2$ water-in-salt electrolyte. *J. Am. Chem. Soc.* **141**, 6338–6344 (2019).
8. Abbas, Q. et al. Strategies to improve the performance of carbon/carbon capacitors in salt aqueous electrolytes. *J. Electrochem. Soc.* **162**, A5148–A5157 (2015).
9. Liu, Q. et al. 2.2V high performance symmetrical fiber-shaped aqueous supercapacitors enabled by "water-in-salt" gel electrolyte and N-doped graphene fiber. *Energy Storage Mater.* **24**, 495–503 (2020).
10. Yoshio, H., Katsuhei, K., Akira, M. & Shin, S. Production of methane and ethylene in electrochemical reduction of carbon dioxide at copper electrode in aqueous hydrogencarbonate solution. *Chem. Lett.* **15**, 897–898 (1986).
11. Tomita, Y., Teruya, S., Koga, O. & Hori, Y. Electrochemical reduction of carbon dioxide at a platinum electrode in acetonitrile-water mixtures. *J. Electrochem. Soc.* **147**, 4164–4167 (2000).
12. Chen, Y.-T., Chen, H.-Y., Chien, Y.-S., Chuang, M.-C. & Chen, P.-Y. An excellent anode renders protic ionic liquids sustainable in metal electrodeposition. *Green Chem.* https://doi.org/10.1039/C9GC04169A 2020.
13. Huang, Q. & Lyons, T. W. Electrodeposition of rhenium with suppressed hydrogen evolution from water-in-salt electrolyte. *Electrochem. Commun.* **93**, 53–56 (2018).
14. Pasta, M., Wessells, C. D., Huggins, R. A. & Cui, Y. A high-rate and long cycle life aqueous electrolyte battery for grid-scale energy storage. *Nat. Commun.* **3**, 1149 (2012).
15. Wu, X. et al. Diffusion-free Grotthuss topochemistry for high-rate and long-life proton batteries. *Nat. Energy* **4**, 123–130 (2019).
16. Wessells, C., Ruffo, R., Huggins, R. A. & Cui, Y. Investigations of the electrochemical stability of aqueous electrolytes for lithium battery applications. *Electrochem. Solid State Lett.* **13**, A59–A61 (2010).
17. Winter, M. The solid electrolyte interphase – the most important and the least understood solid electrolyte in rechargeable Li batteries. *Z. Phys. Chem.* **223**, 1395–1406 (2009).
18. Wood, S. M. et al. Predicting calendar aging in lithium metal secondary batteries: the impacts of solid electrolyte interphase composition and stability. *Adv. Energy Mater.* **8**, 1801427 (2018).
19. Cheng, D. et al. Unveiling the stable nature of the solid electrolyte interphase between lithium metal and LiPON via cryogenic electron microscopy. *Joule* **4**, 2484–2500 (2020).
20. Li, W. & Dahn, J. R. Lithium-ion cells with aqueous electrolytes. *J. Electrochem. Soc.* **142**, 1742–1746 (1995).
21. Suo, L. et al. How solid-electrolyte interphase forms in aqueous electrolytes. *J. Am. Chem. Soc.* **139**, 18670–18680 (2017).
22. Zhao, M., Song, X., Wang, F., Dai, W. & Lu, X. Electrochemical performance of single crystalline spinel $LiMn_2O_4$ nanowires in an aqueous $LiNO_3$ solution. *Electrochim. Acta* **56**, 5673–5678 (2011).
23. Wang, G. J. et al. Electrochemical behavior of $LiCoO_2$ in a saturated aqueous Li_2SO_4 solution. *Electrochim. Acta* **54**, 1199–1203 (2009).
24. Liu, X.-H., Saito, T., Doi, T., Okada, S. & Yamaki, J.-I. Electrochemical properties of rechargeable aqueous lithium ion batteries with an olivine-type cathode and a NASICON-type anode. *J. Power Sources* **189**, 706–710 (2009).
25. Chen, Y., Freunberger, S. A., Peng, Z., Bardé, F. & Bruce, P. G. Li–O_2 battery with a dimethylformamide electrolyte. *J. Am. Chem. Soc.* **134**, 7952–7957 (2012).
26. Khurram, A., He, M. & Gallant, B. M. Tailoring the discharge reaction in Li-CO_2 batteries through incorporation of CO_2 capture chemistry. *Joule* **2**, 2649–2666 (2018).
27. Yao, K. P. C. et al. Thermal stability of Li_2O_2 and Li_2O for Li-air batteries: in situ XRD and XPS studies. *J. Electrochem. Soc.* **160**, A824–A831 (2013).
28. Dong, Q. et al. Cathodically stable Li-O_2 battery operations using water-in-salt electrolyte. *Chem* **4**, 1345–1358 (2018).
29. Ding, M. S. & Xu, K. Phase diagram, conductivity, and glass transition of LiTFSI–H_2O binary electrolytes. *J. Phys. Chem. C* **122**, 16624–16629 (2018).
30. Frost, R. L. & Palmer, S. J. Infrared and infrared emission spectroscopy of nesquehonite $Mg(OH)(HCO_3)\cdot 2H_2O$–implications for the formula of nesquehonite. *Spectrochim. Acta A* **78**, 1255–1260 (2011).
31. Nunn, P. B. & O'Brien, P. The interaction of β-*N*-methylamino-L-alanine with bicarbonate: an ^{1}H-NMR study. *FEBS Lett.* **251**, 31–35 (1989).
32. Abbott, T. M., Buchanan, G. W., Kruus, P. & Lee, K. C. ^{13}C nuclear magnetic resonance and Raman investigations of aqueous carbon dioxide systems. *Can. J. Chem.* **60**, 1000–1006 (1982).

33. Jakobsen, J. P., Krane, J. & Svendsen, H. F. Liquid-phase composition determination in CO_2–H_2O–alkanolamine systems: an NMR study. *Ind. Eng. Chem. Res.* **44**, 9894–9903 (2005).
34. Fears, T. M. et al. Evaluating the solid electrolyte interphase formed on silicon electrodes: a comparison of *ex situ* X-ray photoelectron spectroscopy and *in situ* neutron reflectometry. *Phys. Chem. Chem. Phys.* **18**, 13927–13940 (2016).
35. Dubouis, N. et al. The role of the hydrogen evolution reaction in the solid–electrolyte interphase formation mechanism for "*Water-in-Salt*" electrolytes. *Energy Environ. Sci.* **11**, 3491–3499 (2018).
36. Jiang, L. et al. High-voltage aqueous Na-ion battery enabled by inert-cation-assisted water-in-salt electrolyte. *Adv. Mater.* **32**, 1904427 (2020).
37. Huang, J. & Rüther, T. Why are ionic liquids attractive for CO_2 absorption? An overview. *Aust. J. Chem.* **62**, 298–308 (2009).
38. Cadena, C. et al. Why is CO_2 so soluble in imidazolium-based ionic liquids? *J. Am. Chem. Soc.* **126**, 5300–5308 (2004).
39. Tan, P. et al. Solid-like nano-anion cluster constructs a free lithium-ion-conducting superfluid framework in a water-in-salt electrolyte. *J. Phys. Chem. C* **125**, 11838–11847 (2021).

Methods

Preparation of WIS and SIW electrolytes. LiTFSI (>98%, TCI) and water (HPLC grade, Alfa) were used as received. Aqueous electrolytes of WIS (21 m LiTFSI) and SIW (5 m LiTFSI) were prepared at the desired molalities (moles salt in kilogram solvent).

Preparation of CO_2-rich electrolytes. The CO_2-rich electrolyte was obtained as follows. First, 3 ml of the 5 m SIW solution in a glass container was vacuumed, then purged with Ar gas for ten minutes and finally treated by CO_2 at a flow rate of 10 ml min^{-1} for one hour.

Electrolyte characterization. The pH of different solutions was obtained by a pH meter (Smart Sensor, pH 818). FTIR spectra were recorded on a Bruker VERTEX 70v spectrometer. The ^{17}O, ^{19}F, ^{1}H and ^{13}C NMR spectra were acquired on a Bruker DRX 500 spectrometer, the reference compound was deuterium oxide. The ionic conductivity was obtained by standard conductivity cells (Shanghai Russell Technology). The conductivity constant was predetermined using 1 M aqueous KCl standard solution at 25 °C. The ionic conductivities of the electrolytes were obtained from electrochemical impedance spectroscopy using an electrochemical workstation (Zahner IM6) in an oven at a set temperature. Viscosity was measured by an MCR 502 Anton Paar with a controlled shear rate and shear stress at 20 °C. Differential scanning calorimetry was performed by a DSC1 (Mettler-Toledo) from −100 °C to 90 °C at a heating rate of 2 °C min^{-1}, and the sample was kept at −100 °C for 5 minutes before testing.

Electrochemical measurements of various gas reductions in WIS. A three-electrode device supplied with continuous gas flow (CO_2, O_2, air or Ar) was set up in an Ar atmosphere (Ar glove box). The 21 m WIS electrolytes (6.5 ml) were vacuumed in a vacuum oven before use. The three-electrode device was assembled with Mo_6S_8 on Ti mesh as the working electrode (~2 mg, 8 mg cm^{-2}), activated carbon (~20 mg, 20 mg cm^{-2}) on Al mesh as the counter electrode and Ag/AgCl as the reference electrode. Both the working and counter electrodes consisted of the active material, super P and PTFE at a weight ratio of 8:1:1.

Electrochemical measurements of the full-cell ($LiMn_2O_4$/CO_2–SIW/Mo_6S_8). The soft-packaged battery was assembled with a $LiMn_2O_4$ electrode (8 mg cm^{-2}; thick electrode, 40 mg cm^{-2}; $LiMn_2O_4$/graphite/carbon-black/PTFE, 80:10:2:8) and Mo_6S_8 electrode (5 mg cm^{-2}; thick electrode, 40 mg cm^{-2}; Mo_6S_8/activated-carbon/carbon-black/graphite/PTFE, 70:15:7:3:5). The electrolyte volume used was 80 µl (for the thick electrode, 150 µl). Titanium mesh (80 mesh) coated by carbon film was used as the current collector for the cathode, and aluminium mesh (200 mesh) for the anode. Glass fibre (Whatman D) was used as a separator. The electrochemical impedance spectroscopy was performed on an electrochemical workstation (Zahner IM6) with A.C.C signals of 5 mV amplitude in the frequency range of 1 Hz−6.0 MHz, and the galvanostatic charge–discharge test was performed using a Neware (BTS 7.6.X) battery testing system.

CO_2 content titration experiment. The CO_2 contents in electrolytes were determined by a chemical titration experiment at room temperature. First, NaOH solution (pH, 10.5) and HCl solution (0.01 m l^{-1}) were prepared according to the concentration ratio, and deionized water was boiled before being used as a solvent to remove the initial CO_2 inside it; methyl orange solution (1 mg ml^{-1}) was used as the titration indicator. Then 1 ml electrolyte was mixed with 10 ml NaOH solution; the dissolved CO_2 reacted with the NaOH solution ($CO_2 + 2NaOH = Na_2CO_3 + H_2O$, equation (1)), forming sodium carbonate (Na_2CO_3); after adding three drops of indicator into the mixed solution, the aqueous solution containing Na_2CO_3 and residual NaOH was finally titrated by adding a known concentration of HCl (0.01 m l^{-1}; $NaOH + HCl = NaCl + H_2O$, equation (2); $Na_2CO_3 + 2HCl = 2NaCl + H_2O + CO_2$, equation (3)). The volume of HCl consumed was recorded as V_1, and the volume of HCl consumed in 10 ml bare NaOH solution was recorded as V_2; the amount of HCl consumed due to the dissolved CO_2 (n) in the solution can be given as $n = (V_1 - V_2) \times 0.01$. Finally, the CO_2 content can be obtained according to the reaction in equation (3). All the samples were measured three times to get the mean value.

Molecular dynamics simulation. Classical molecular dynamics simulations were conducted to investigate the effect of CO_2 on the NMR spectrum of F for LiTFSI solution. The OPLS force field was used for the Li^+ ion, and the CL&P force field was employed for $TFSI^-$, which can capture structure information in LiTFSI solution[40–42]. The SPC/E model was adopted for water[43], and the force field for CO_2 was taken from ref. [44]. The effect of CO_2 on the NMR spectrum of F for LiTFSI electrolytes was scrutinized in four different concentrations (5 m, 10 m, 15 m and 21 m). The simulation system is shown in Supplementary Fig. 39, and the number of each type of ion/molecule is given in Supplementary Table 3 for all systems.

Data availability

All the data generated or analysed during this study are included in this article and its Supplementary Information. The details of the molecular dynamics simulation are available in Supplementary Data 1. Source data are provided with this paper.

References

40. Jorgensen, W. L., Maxwell, D. S. & Tirado-Rives, J. Development and testing of the OPLS all-atom force field on conformational energetics and properties of organic liquids. *J. Am. Chem. Soc.* **118**, 11225–11236 (1996).
41. Canongia Lopes, J. N. & Pádua, A. A. H. Molecular force field for ionic liquids composed of triflate or bistriflylimide anions. *J. Phys. Chem. B* **108**, 16893–16898 (2004).
42. McEldrew, M., Goodwin, Z. A. H., Kornyshev, A. A. & Bazant, M. Z. Theory of the double layer in water-in-salt electrolytes. *J. Phys. Chem. Lett.* **9**, 5840–5846 (2018).
43. Berendsen, H. J. C., Grigera, J. R. & Straatsma, T. P. The missing term in effective pair potentials. *J. Phys. Chem.* **91**, 6269–6271 (1987).
44. Zhu, A., Zhang, X., Liu, Q. & Zhang, Q. A fully flexible potential model for carbon dioxide. *Chin. J. Chem. Eng.* **17**, 268–272 (2009).

Acknowledgements

All authors except K.X. acknowledge the support of the National Natural Science Foundation of China (51872322) and the Center for Clean Energy. J.Z., M.C. and G.F. thank the Hubei Provincial Natural Science Foundation of China (2020CFA093) and the Program for Huazhong University of Science and Technology, Academic Frontier Youth Team. K.X. thanks the Joint Center of Energy Storage Research, an energy hub funded by the US Department of Energy, Basic Energy Sciences, for support.

Author contributions

L.S. and K.X. conceived the idea. J.Y. and L.S. designed the experiments. J.Y. performed the material preparation, electrochemical measurements and data analysis. L.J. performed the NMR measurements. Y.T. collected the TEM images, and L.L. measured the XPS spectra. T.L. performed the cost analysis of the electrolyte. J.Z., M.C. and G.F. performed the molecular dynamics simulations and analysed the data. J.Y., G.F., K.X. and L.S. wrote the manuscript. All authors discussed the results and commented on the manuscript.

Competing interests

The authors declare no competing interests.

Additional information

Supplementary information The online version contains supplementary material available at https://doi.org/10.1038/s41557-021-00787-y.

Correspondence and requests for materials should be addressed to Kang Xu or Liumin Suo.

Peer review information *Nature Chemistry* thanks Jin Han and the other, anonymous, reviewer(s) for their contribution to the peer review of this work.